Descriptive tools for the analysis of texture projects with large datasets using MTEX: strength, symmetry and components

David Mainprice, Florian Bachmann, Ralf Hielscher, Helmut Schaeben

Descriptive tools for the analysis of texture projects with large datasets using MTEX: strength, symmetry and components

DAVID MAINPRICE[1]*, FLORIAN BACHMANN[2], RALF HIELSCHER[3] & HELMUT SCHAEBEN[2]

[1]*Geosciences Montpellier UMR CNRS 5243, Université Montpellier 2, 34095 Montpellier Cedex 05, France*

[2]*Mathematische Geologie und Geoinformatik, Institut für Geophysik und Geoinformatik, Technische Universität Freiberg, 09596 Freiberg, Germany*

[3]*Fakultät für Mathematik, Technische Universität Chemnitz, 09126 Chemnitz, Germany*

**Corresponding author (e-mail: David.Mainprice@gm.univ-montp2.fr)*

Abstract: This paper presents the background for the calculation of various numbers that can be used to characterize crystal-preferred orientation (CPO), also known as texture in materials science, for large datasets using the combined scripting possibilities of MTEX and MatLab®. The paper is focused on three aspects in particular: the strength of CPO represented by orientation and misorientation distribution functions (ODFs, MDFs) or pole figures (PFs); symmetry of PFs and components of ODFs; and elastic tensors. The traditional measurements of texture strength of ODFs, MDFs and PFs are integral measurements of the distribution squared. The M-index is a partial measure of the MDF as the difference between uniform and measured misorientation angles. In addition there other parameters based on eigen analysis, but there are restrictions on their use. Eigen analysis does provide some shape factors for the distributions. The maxima of an ODF provides information on the modes. MTEX provides an estimate of the lower bound uniform fraction of an ODF. Finally, we illustrate the decomposition of arbitrary elastic tensor into symmetry components as an example of components in anisotropic physical properties. Ten examples scripts and their output are provided in the appendix.

One of the major objects of quantitative texture analysis is to provide standard procedures to allow the numerical comparison between samples. Standard texts such as Bunge (1969, 1982), Matthies *et al.* (1987) and Engler & Randle (2010) present the mathematical background of classical texture analysis. Almost all the early theoretical and mathematical development of quantitative texture analysis was driven by requirements of metal forming in material science, with the exception of some contributions from spherical statistics (e.g. Fisher 1953; Watson 1966; Mardia 1972; Bingham 1974; Watson 1983). Many students in Earth sciences (and probably some in materials sciences) are not often exposed to the theoretical and mathematical development of quantitative texture analysis as they have access to modern automated texture acquisition equipment; the most widely available are electron backscattered diffraction (EBSD) systems on scanning electron microscopes (SEMs) in most university electron microscopy centres. In this paper we provide some basic background to the quantities characterizing texture and procedures, which we will present as MTEX scripts. The increasing acquisition speed of EBSD in recent years has caused a dramatic increase in the size of individual sample data files and the number of specimens studied; it is now not uncommon for 20–50 samples to be studied for a single project. With this increase of data there is a need to study many samples in a coherent way and analyse the trends for various characteristics for strength, symmetry and components. The characteristics chosen to analyse and describe large datasets or databases will depend on the objectives of the project. MTEX provides a unique means for the customized quantitative texture analysis of large multi-file projects as the MatLab® environment uses a scripted language and a complex analysis can be developed in a m-file, which can evolve with changing requirements of the project.

This paper is designed as a reference for Earth and material scientists who want to use the MTEX texture analysis software to apply the methods presented in this paper. MTEX is a comprehensive open-source freely available MatLab® toolbox that covers a wide range of problems in quantitative texture analysis, for example, ODF modelling, pole figure to ODF inversion, EBSD data analysis, grain modelling and anisotropic physical properties

(Hielscher & Schaeben 2008; Bachmann *et al.* 2010; Bachmann *et al.* 2011; Mainprice *et al.* 2011). The MTEX toolbox can be downloaded from http://mtex.googlecode.com. Unlike many other texture analysis software, it provides a programming interface which allows for the efficient processing of complex research problems in the form of scripts (m-files). The MatLab® environment provides a wide variety of high-quality graphics file formats to aid publication and display of the results. In addition, the MTEX toolbox will work identically on Microsoft Windows, Apple Mac OSX and Linux platforms in 32- and 64-bit modes with a simple installation procedure.

In MTEX texture analysis information such as ODFs, EBSD data and pole figures are represented by variables of different types. For example, in order to define a unimodal ODF with half-width 10°, modal preferred orientation (10−30°) in Euler angles and orthorhombic crystal symmetry of *mmm*, the command which generates a variable myODF of type ODF is issued, which is displayed as a script and output in Appendix I. We use this style of displaying script and the output of each script in the appendix to make the syntax of MTEX as clear as possible. Note that there is also an exhaustive interactive documentation included in MTEX, which explains the syntax of each command in detail.

Reference datasets

To illustrate the descriptive tools we use three datasets: (1) a visco-plastic self-consistent (VPSC) model of the development of olivine CPO in simple shear; (2) the classical olivine CPO database with a 110 samples of Ben Ismaïl & Mainprice (1998); and (3) the detailed study with 57 samples measured using state-of-the-art EBSD measurements of the crust−mantle transition zone of the Oman Ophiolite. We will now briefly describe these datasets.

VPSC modelling is now well established as robust method for studing CPO development in minerals undergoing plastic deformtion for all types of strain histories (e.g. Tommasi *et al.* 2000; Bascou *et al.* 2002; Ulrich & Mainprice 2005). Here we present the classic case of the development of olivine CPO under progressive simple shear straining using the code developed by Lebensohn & Tomé (1993), with a constant strain increment of 0.025, a grain interaction parameter α of 100 (see Tommasi *et al.* 2000 for discussion) and a velocity gradient tensor (L_{ij}) for simple shear with $L_{12} = 1$ and all other values equal to zero. The initial CPO is composed of 1000 random orientations ('grains'). We have chosen to model an olivine A-type CPO (major slip system is [100](010)), which is the most abundant olivine CPO type in natural samples (Ben Ismaïl & Mainprice 1998). Tommasi *et al.* (2000) give an extensive introduction of VPSC modelling of olivine CPO; we have used their parameterization for olivine slip systems given in their table 2, with the slip systems having critical resolved shear stress (CRSS) values of 1 for (010)[100] and (001)[100], 2 for (010)[001], 3 for (100)[001], 4 for {011}[100] and {031}[100] and 6 for {110}[001]. A low value of CRSS signifies an easy slip system; (010)[100] is six times easier than {110}[001]. The advantage of the VPSC model for the present study is that it provides the evolution of the CPO as function of finite shear strain (Fig. 1). VPSC model data also have no 'noise', associated with more complex microstructures and deformation histories of naturally deformed samples.

The olivine database of Ben Ismaïl & Mainprice (1998) has become a reference for the CPO of naturally deformed olivine in upper mantle rocks. The database contains 110 olivine CPO measured using the universal stage with 100 grains per sample. Although the number of grains is relatively small compared to modern EBSD studes, the universal stage data are very reliable and represents over 30 years of olivine studies from a large range of geodynamic environments. The advantage of this dataset is it contains many different olivine CPOs, but is dominated by A-type CPO which we have simulated using the VPSC model.

The data published by Higgie & Tommasi (2012) are high-quality EBSD data with many thousands of grains per sample. The sample area was restricted to an 80 m vertical section of the crust−mantle transition zone in the Oman Ophiolite. In the 57 samples taken from the 80 m section there is an olivine CPO transition from axial-[100] symmetry ([100] has a pole figure with a point maxima and all other pole figures are girdles, also know as [100] fibre texture) to axial-[010] symmetry. The main advantages of this dataset are that there is a CPO symmetry transition from axial-[100] to axial-[010] and the number of samples and EBSD data points are very high from a small field area.

Strength

When studying crystal-preferred orientation (CPO), one of the first questions is how strong is the CPO of my specimen? To answer this question you have to decide which phase of your polyphase specimen you want to study, as all the methods we will introduce apply to a single phase with a specified crystal symmetry. In traditional quantitative

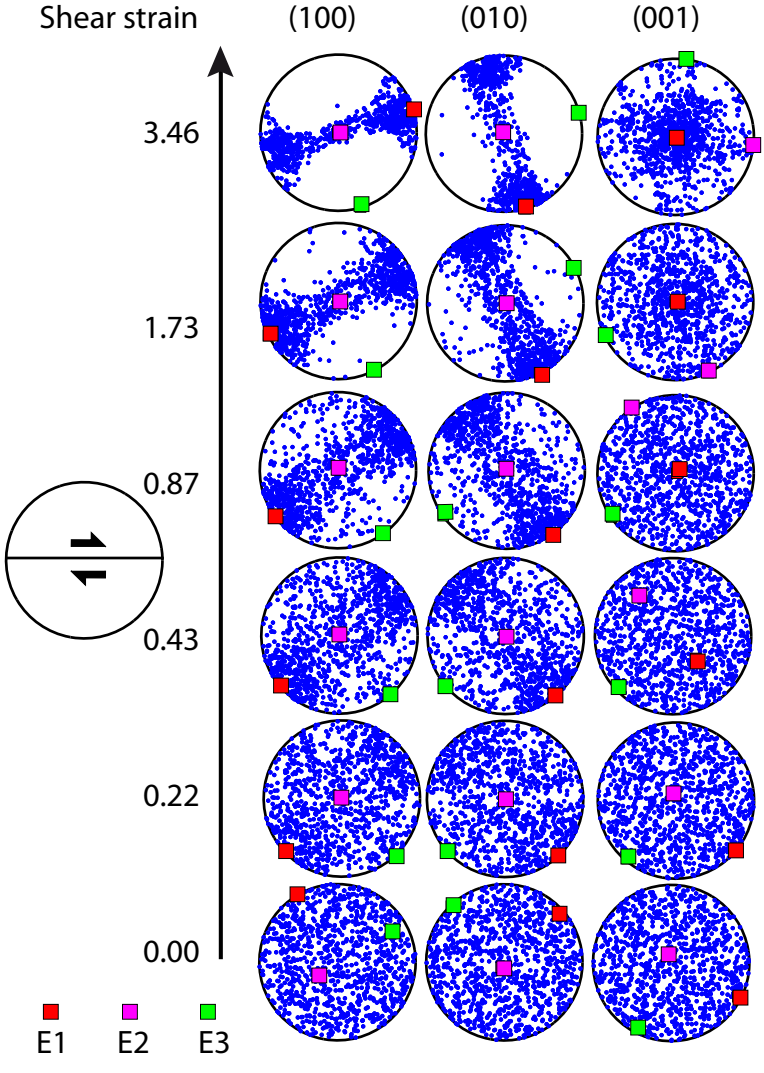

Fig. 1. Evolution of olivine VPSC model CPO presented as pole figures of the 1000 individual orientations as a function of shear strain. The arrows indicate the shear sense on the shear plane. Note the shear strain scale is not linear. E1, E2 and E3 are eigenvectors of the orientation tensor for each individual pole figure, where the eigenvalues (λ_1, λ_2, λ_3) corresponding to the vectors have magnitudes $\lambda_1 \geq \lambda_2 \geq \lambda_3$. The eigen analysis is discussed later in the text.

texture analysis, this question is typically answered by either looking at a specific peak in the ODF associated with a texture component or the texture index of the ODF. The ODF is the first choice because the ODF contains all the crystal orientation information and its total volume is defined by the crystal symmetry and specimen symmetry. The definition of the ODF is made by ignoring the shape, position and grain size of the crystals and just considering their orientation. Typically an orientation is defined by three Euler rotation angles φ_1, Φ and φ_2 as defined by Bunge (1982), referring to successive rotations about z, x, z. Often we use the letter g to represent an orientation and $V(g)$ its volume portion in the ODF. Often for data such as EBSD maps composed of gridded diffraction points we will assume $V(g) = 1$ as diffraction volume is the same for all points. We define $\Delta V(g)$ as the volume portion of all crystals, not necessarily adjacent crystals, having orientations within an (infinitesimal) volume element dg of g, and V as the total volume for all the crystals of this phase

for the whole sample. The ODF for the most general case of triclinic crystal and triclinic specimen symmetry is then $f(g)$ in

$$\frac{\Delta V(g)}{V} = f(g)\,\mathrm{d}g,$$

where $\mathrm{d}g = \sin\Phi\,\mathrm{d}\varphi_1\,\mathrm{d}\Phi\,\mathrm{d}\varphi_2/8\pi^2$ is the rotationally invariant volume element of the orientation manifold with respect to which ODFs are normalized. Since the uniform ODF is $f \equiv 1$, an ODF is expressed in multiples of the uniform distribution, sometimes abbreviated as 'mud'. Notice the ODF is a density function in terms of volume fraction of crystals in a given orientation range; the traditional quantitative texture analysis is therefore expressed in volume fractions. When using EBSD maps with gridded diffraction points in spacing less than the grain size, using all indexed points should give a reasonable representative area (depending on the spacing) for the grains and the correct area fraction weighting for the ODF and all subsequent analysis that uses the ODF. If we take the EBSD map points and model the grain structures by whatever process, we should obtain the average orientation of the grain and a weighting proportional to the grain area. If we use the popular 'one point per grain model' without the area weighting, this is not traditional quantitative texture analysis as weighting is set to 1 for all grains with different areas. This approach may be useful for a specific project, for example when studying nucleation and grain growth. The volume fraction approach of traditional quantitative texture analysis is appropriate for physical property calculations, whereas the 'one point per grain model' is not.

Having established the definition of an ODF we can define the texture index of ODF as

$$J_{\mathrm{ODF}} = \int |f(g)|^2\,\mathrm{d}g = \|f\|^2_{L^2}.$$

Note that the definition of J_{ODF} involves the square of f; this type of functional is called a L^2-norm. For a uniform distribution $J_{\mathrm{ODF}} = 1$ and for a single orientation J_{ODF} will have an infinitely large value. For a given combination of crystal symmetry, specimen symmetry and ODF kernel function with given half-width, the bell-shaped spread for a single orientation will have a corresponding maximum value. As an example, the ODFs in a script are defined by their crystal symmetry (CS), specimen symmetry (SS) and a single orientation (unimodal ODF) for a single crystal of olivine and plagioclase felspar An80, respectively, and the texture indices J_{ODF} are calculated for both ODFs. The example uses the recommended and default `MTEX` de la Vallee Poussin kernel to represent ODFs for CPO studies (example script and output in Appendix II).

From the output we can see the texture index for the unimodal orientation distribution for olivine is 140.01 and for plagioclase is 560.05; the specimen symmetry is the triclinic for both ODFs. The ratio of the texture indices plagioclase/olivine is 4 due to different volumes of Euler angle manifold for plagioclase (CS triclinic) and olivine (CS orthorhombic). The domain of the Euler angle manifold using Bunge's Euler angles in degrees is $[0, 360) \times [0, 180] \times [0, 360)$ for triclinic and $[0, 180) \times [0, 180] \times [0, 180)$ for orthorhombic crystal symmetry. Since the volume is $\int \sin\Phi\,\mathrm{d}\varphi_1\,\mathrm{d}\Phi\,\mathrm{d}\varphi_2/8\pi^2$ over the corresponding domains, the volume ratio of ODFs plagioclase (CS triclinic) and olivine (CS orthorhombic) is $8\pi^2/2\pi^2 = 4$. Comparing the texture indices J_{ODF} of ODFs of different symmetry is therefore not recommended unless a correction for the volume of the ODFs is made. For broader unimodal orientation distributions, the required correction is not as simple as in the example above.

In an almost identical way we can define the misorientation distribution function (MDF). The misorientation $\tilde{g}$ is the difference between two orientations g_1 and g_2 and is defined as $\tilde{g} = g_1^{-1}g_2$ such that $g_1\tilde{g} = g_2$. The MDF $f_{\mathrm{MDF}}(\tilde{g})$ is then defined for the two orientations with triclinic crystal symmetry by

$$\frac{\Delta V(\tilde{g})}{V} = f_{\mathrm{MDF}}(\tilde{g})\,\mathrm{d}\tilde{g},$$

where $\mathrm{d}\tilde{g}$ is the same rotationally invariant volume element of the orientation manifold. We can define the texture index of a MDF as

$$J_{\mathrm{MDF}} = \int |f_{\mathrm{MDF}}(\tilde{g})|^2\,\mathrm{d}\tilde{g} = \|f_{\mathrm{MDF}}\|^2_{L^2}.$$

As seen before, J_{MDF} involves the square of f_{MDF} and this type of functional is called the L^2-norm. For a uniform distribution J_{MDF} is 1; for a unimodal misorientation distribution J_{MDF} will have a maximum value. In the case of MDF the specimen symmetry does not apply to the misorientation Euler manifold, which is uniquely defined by the crystal symmetry of g_1 and g_2. In the simplest case the two misorientations have the same crystal symmetry; for olivine with orthorhombic symmetry the MDF domain using Bunge's Euler angles is $[0, 90) \times [0, 90] \times [0, 180)$, whereas for the ODF it is $([0, 180) \times [0, 180] \times [0, 180))$. We can repeat the above exercise for olivine and plagioclase, but this time using the calcMDF with the option

'uncorrelated' as we have not associated specimen co-ordinates with g_1 and g_2 and using the ODFs of two modal orientations (see example script and output in Appendix III).

The texture index values for the olivine and plagioclase MDFs are 49.32 and 197.39 respectively, whereas for the ODFs they are 140.01 and 560.05. As for the ODF, the maximum value for a unimodal misorientation distribution depends on the domain and the volume of the Euler angle manifold; the larger the volume the larger the texture index value. As the ODF (depending on specimen and crystal symmetry) generally has a larger domain than the MDF (depending on crystal symmetries of g_1 and g_2), texture indices for $J_{\mathrm{ODF}} > J_{\mathrm{MDF}}$ for pronounced unimodal ODF and its uncorrelated MDF.

A characteristic introduced into quantitative texture analysis by Schaeben (1988) is the entropy of an ODF (or MDF). The entropy of an ODF is defined as

$$S_{\mathrm{ODF}} = -\int f(g)\,\ln f(g)\,\mathrm{d}g.$$

Whereas the texture index is a measure of strength or concentration, the entropy is a measure of the deviation from the uniform ODF which quantifies the dispersion of orientations within the ODF. $S_{\mathrm{ODF}} = 0$ for the uniform ODF and has a minimum (negative) value for a unimodal orientation. The entropy involving the ln function responds very sensitively to small values of an ODF, while the texture index involving squaring responds very sensitively to large values of an ODF. Hielscher *et al.* (2006) have shown that the S_{ODF} is related to J_{ODF} by

$$-\ln J_{\mathrm{ODF}} \leq S_{\mathrm{ODF}} \leq 0.$$

We discuss the implications of this relationship in the section 'Components'.

Another CPO strength characteristic based on the misorientation angle distribution, introduced by Skemer *et al.* (2005), is called the *M*-index. The method is based on the difference between the theoretical uniform distribution and the measured uncorrelated misorientation angle distributions for a given crystal symmetry class. The theoretical uniform distribution can be analytically calculated using Rodrigues vectors (Morawiec 2004) or quaternions (Grimmer 1979). The *M*-index in terms of continuous misorientation angle density for the uniform distribution $f^{(U)}(\theta)$ and measured $f^{(M)}(\theta)$ can be defined

$$M = \frac{1}{2}\int |f^{(U)}(\theta) - f^{(M)}(\theta)|\,\mathrm{d}\theta = \frac{1}{2}\left\|f^{(U)} - f^{(M)}\right\|_{L^1},$$

whereas Skemer *et al.* (2005) used a discrete approach with a look-up table for the uniform distribution $D_i^{(U)}$ and a histogram with bins of 1° for measured distribution $D_i^{(M)}$, defined

$$M = \frac{\theta_{\max}}{2n}\sum_{i=1}^{n} |D_i^{(U)} - D_i^{(M)}|.$$

The *M*-index is the L^1-norm of the difference. It does not involve a squared function as for J_{ODF} and J_{MDF}. The L^1-norm of the difference between any two probability density functions measures the probability mass that is differently distributed by the two densities. The *M*-index only uses the marginal angle distribution of the misorientation distribution function (MDF), as any misorientation can be decomposed into a rotation axis and angle and only the angle is used to calculated the *M*-index. As the discrete approach has already been described by Skemer *et al.* (2005), we illustrate how to calculate the *M*-index using the continuous functions with `MTEX`. The following four steps are required:

(1) calculate the uniform misorientation angle distribution for crystal symmetry of your mineral;
(2) calculate the uncorrelated MDF from the ODF;
(3) calculate uncorrelated misorientation angle distribution from MDF; and
(4) calculate the *M*-index (see example script in Appendix IV).

J_{ODF}, J_{MDF} and *M*-index are plotted as a function of shear strain in Figure 2, representing the continuous evolution of the CPO with progressive plastic deformation using the VPSC model data presented earlier. Figure 2 shows the results with a progressively increasing value for all three characteristics. Both J_{ODF} and J_{MDF} are normalized such that uniform distribution has a value of 1. The 1000 orientations ('grains') of the starting CPO have J_{ODF} and J_{MDF} values of 1.13 and 1.00, respectively. The *M*-index characteristic is normalized to have value 0 for a uniform distribution and the starting CPO has a value of 0.00. The maximum value for a shear strain is also quite different for J_{ODF}, J_{MDF} and *M*-index, being 7.84, 2.51 and 0.31, respectively, corresponding to ranges of 6.71, 1.51 and 0.31. J_{ODF} has a range that is 4.44 times that of J_{MDF} and 21.64 times that of the *M*-index characteristic. The curvature of the evolution of J_{ODF} and J_{MDF} with shear strain is concave to the top, whereas the *M*-index is slightly convex to the top. The ODF-related characteristic J_{ODF} has a much larger range than the uncorrelated-MDF-related characteristics

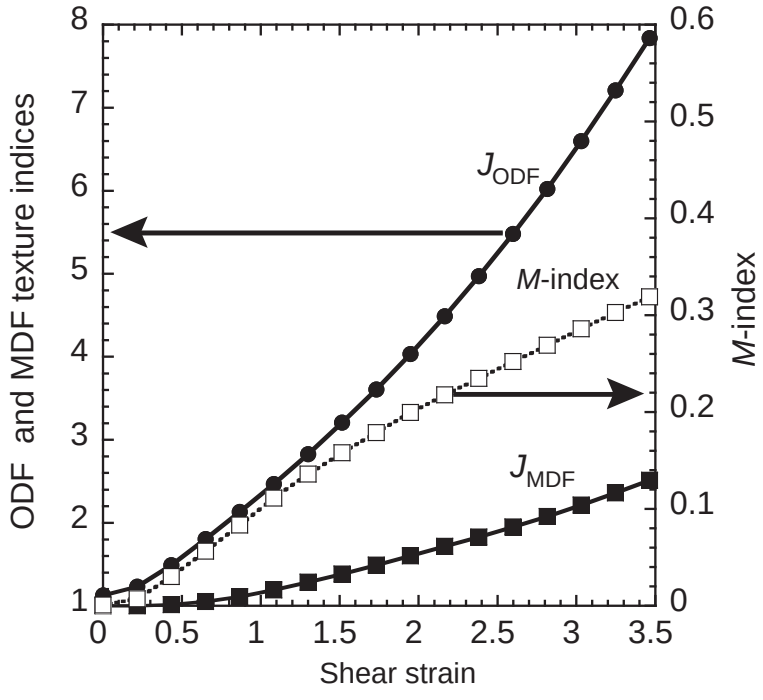

Fig. 2. CPO strength characteristics for olivine CPOs from a VPSC simulation where J_{ODF} and J_{MDF} are the texture indices of the ODF and MDF, respectively, and M-index is an index of uncorrelated misorientation angle distribution. The scale on the left is for J_{ODF} and J_{MDF} and on the right for M-index.

J_{MDF} and M-index, which is directly related to the fact that the uncorrelated MDF is an autocorrelated function of the ODF and has a smaller total Euler angle volume, hence a smaller normalized amplitude.

Earth scientists in general prefer pole figures to represent CPO rather than ODFs or MDFs. Pole figures have the advantage of being plotted in the specimen reference frame and can be easily related to structural features, such as grain-shaped defined lineation and foliation. For unit axes $\pm\boldsymbol{h}$ and unit directions $\boldsymbol{r}$ we define the pole density in terms of a Radon transform of the ODF f:

$$P(\pm\boldsymbol{h}, \boldsymbol{r}) = \frac{1}{2\pi}\int_{\{\pm g\boldsymbol{h}=\boldsymbol{r}\}} f(g)\,\mathrm{d}g.$$

Since $\pm\boldsymbol{h}$ is a unit axis given in crystal coordinates, we consider it as a parameter rather than a variable; $P(\boldsymbol{h}, \circ)$ is then referred to as pole figure. Since $\boldsymbol{r}$ is a unit direction given in specimen coordinates, it is referred to as a parameter and $P(\circ, \boldsymbol{r})$ is referred to as inverse pole figure. Unit vectors can be expressed in spherical polar angles (α, β), the polar angle $\alpha \in [0, 180]$ and the azimuthal angle $\beta \in [0, 360)$. We can then define a texture index for the $\boldsymbol{h}$-pole figure $P(\boldsymbol{h}, \circ)$ as

$$J_{\mathrm{PF}} = \int |P(\boldsymbol{h}, \boldsymbol{r})|^2\,\mathrm{d}r = \ \|P\|^2_{L^2}$$

with the rotationally invariant (infinitesimal) surface element $\mathrm{d}\boldsymbol{r} = \sin\alpha d\alpha d\beta/4\pi$ of the unit sphere, which makes J_{PF} a rotationally invariant functional of P.

For the uniform ODF $f = 1$ the pole density $P(\boldsymbol{h}, \boldsymbol{r}) = 1$ for all $\boldsymbol{r}$ and any $\boldsymbol{h}$ with $J_{\mathrm{PF}} = 1$. The value of J_{PF} will be a maximum for a single orientation g with the same conditions as the ODF and MDF above for a given combination of crystal symmetry, specimen symmetry, ODF kernel function and half-width; in addition, it will vary with the crystal multiplicity of $\pm\boldsymbol{h}$. Multiplicity is a function of the crystal symmetry as it refers to the total number of symmetrically equivalent crystallographic axes or poles $\pm\boldsymbol{h}$. The simplest case is triclinic symmetry with a multiplicity of 1. Higher symmetries all have some multiplicities larger than 1 depending on the specific direction or pole considered.

Consider the case of a single orientation of α-quartz crystal symmetry and the pole figures of

$\boldsymbol{c}(0001)$, $\boldsymbol{a}(2\bar{1}\bar{1}0)$, $\boldsymbol{m}(10\bar{1}0)$, $\boldsymbol{r}(10\bar{1}1)$ and $\boldsymbol{z}(1\bar{1}01)$. The multiplicity of the poles in the orientation sphere (both hemispheres) are $c = 2$, $a = 3$, $m = 6$, $r = 6$ and $z = 6$ (Fig. 3). Using example script in Appendix V we calculate for each pole figure the maximum pole figure density J_{PF}, the multiplicity m and the product $m \times J_{\mathrm{PF}}$. See example script and output in Appendix V for further details.

From the small table of results produced by the script in Appendix V the effect of multiplicity m on the maximum (Max) and J_{PF} is obvious: the pole figure with smallest multiplicity $\boldsymbol{c}(0001)$ has the highest maximum density (J_{pf}) and the pole figures with higher multiplicity $\boldsymbol{m}(10\bar{1}0)$, $\boldsymbol{r}(10\bar{1}1)$ and $\boldsymbol{z}(1\bar{1}01)$ have lower maximum densites (J_{PF}). The intermediate case is the $\boldsymbol{a}(2\bar{1}\bar{1}0)$ pole figure with a multiplicity if the sign of $+\boldsymbol{a}$ and $-\boldsymbol{a}$ is taken into account. If we had used the option 'antipodal' for generating the pole figures then the multiplicity would have been 6, as it would have been for the pole figure recorded by X-ray texture goniometer where the diffracted intensities of $+\boldsymbol{a}(2\bar{1}\bar{1}0)$ and $-\boldsymbol{a}(\bar{2}110)$ are the same due to the diffraction physics (also known as Friedel's law). In MTEX it is possible to consider three-dimensional vectors either as directions with positive and negative signs (also called polar vectors) or as unsigned axes where positive and negative directions are not distinguished (also called non-polar axes). The option 'antipodal' indicates that the vectors, for example pole to planes, are to be treated as axes without sign. Taking $m \times J_{\mathrm{PF}}$ we can see the product is the same for all pole figures. When comparing pole figure maximum densities and J_{PF}, care has to taken to consider the effect of multiplicity. In this simple example the variation of maximum pole figure densities and J_{PF}, that is, the product $m \times \max_{\mathbf{r}} P(\boldsymbol{h}, \boldsymbol{r}) = 91.90$ for all pole figures. However maximum pole figure density is not a good measure of CPO strength in most cases for three reasons: (1) pole figures generally have submaxima and these are not taken into account; (2) J_{PF} is an integral measure of all directions in the pole figure and hence more representative; and (3) maximum values of density functions are not probabilities, whereas integrals of density functions are probabilities. In any case the pole figure itself is only a partial representation of the complete CPO present in the ODF. In an identical manner we can calculate the J_{IPF} of an inverse pole figure, which may be useful in some cases such as uniaxial plastic deformation as the complete information is represented in the inverse pole figure.

Eigen analysis

Other measures of CPO strength based on pole figures have been presented in the literature based on eigenvector and eigenvalue analysis. For this eigen analysis the pole figure data have to be in the form of unit axes $\pm\boldsymbol{n}$ and this is very

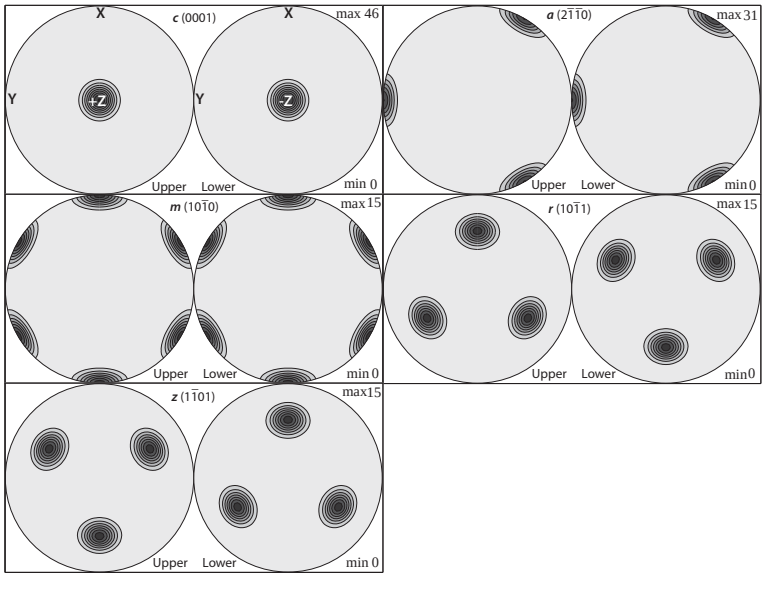

Fig. 3. Single orientation ($\varphi_1 = 0$, $\Phi = 0$, $\varphi_2 = 0$) α-quartz pole figures, upper (left) and lower (right) hemisphere equal area projections. The ODF is calculated with the de la Vallée Poussin kernel with a half-width of 10°.

convenient for studies based on single orientations. Some of the first applications of the eigen method to CPO were made by Watson (1966), Stauffer (1966) and Darot & Bouchez (1976), who were more interested in the symmetry distributions than the CPO strength. The eigen method is based on the orientation tensor T, defined

$$T = \frac{1}{n}\sum_{i=1}^{n} \boldsymbol{n}_i \boldsymbol{n}_i^T = \frac{1}{n}\sum_{i=1}^{n} \begin{pmatrix} x_i x_i & x_i y_i & x_i z_i \\ x_i y_i & y_i y_i & y_i z_i \\ x_i z_i & y_i z_i & z_i z_i \end{pmatrix}$$

where there are unit axes $\pm\boldsymbol{n}_i$ with components $(x_i, y_i, z_i)^{\boldsymbol{T}}$. In MTEX the orientation tensor can be calculated 300 times faster than the summation method above using a row vector $[x, y, z]$ filled with x_i, y_i, z_i. These data can be extracted from an EBSD object for a specific pole $\pm\boldsymbol{h}$ so that $T = 1/n([x, y, z]^T[x, y, z])$ (this method is illustrated in example script in Appendix VI).

Using eigen analysis on structural data, Woodcock (1977) suggested a strength characteristic $C = \ln(\lambda_1/\lambda_3)$ where $C = 0$ to ∞ and λ_1, λ_2 and λ_3 are the eigenvalues of the orientation tensor T where $\lambda_1 \geq \lambda_2 \geq \lambda_3$ and we use the normalization $\lambda_1 + \lambda_2 + \lambda_3 = 1$. Later Lisle (1985) used a characteristic developed by Mardia (1972) and more recently by Mardia & Jupp (2000): $I = (15n/2)(\lambda_1^2 + \lambda_2^2 + \lambda_3^2 - 1/3)$. Unfortunately the equation was misprinted in Lisle (1985) and was reproduced with the error in Vollmer (1990) where the value of I depends on the pole figure symmetry, the maximum value is 5.00 for a perfect point maximum and 0.3125 for a girdle.

For some high crystal symmetries the multiplicity of some crystal directions results in eigen analysis yielding unexpected results. Consider the example of cubic crystal symmetry; the (100)-pole figure of a simple unimodal de la Vallée Poussin ODF has three antipodally symmetric maxima. The eigenvalues are $\lambda_1 = \lambda_2 = \lambda_3 = 1/3$ as they would be in the uniform case. For axes concentrated symmetrically along antipodally symmetric small circles through the space diagonals, the three eigenvalues are again equal. Eigen analysis has its pitfalls when symmetry is present. It is therefore recommended to use eigen analysis of pole figures of low mutiplicity, ideally 1.

Using olivine visco-plastic self-consistent (VPSC) simulation of CPO mentioned previously as our source for the (100)-pole figure, we have plotted all the pole figure characteristics as a function of shear strain (Fig. 4a) and ODF texture index (Fig. 4b). The maximum pole figure density shows the largest range (7.54) of 1.38–8.92. The J_{PF} has a range of 2.98 over 1.02 to 4.00. The C characteristic of Woodcock (1977) has range 3.08 from 0.05 to 3.13. Finally the I characteristic of Mardia (1972) has a starting value of less than zero, a range 2.34 from -0.55 to 1.79. The curvature and the numerical range of all characteristics can be observed in Figure 4, with curvature of J_{PF} and I being similar. We still recommend using the integral characteristics J_{ODF} and J_{PF}, as they sample the completely filled and empty spaces of the ODF and pole figure respectively.

Symmetry

For many aspects of sciences, symmetry is an effective way to characterize an object. The theoretical connection between symmetry and material properties has been studied for nearly 120 years (Curie 1894); CPO is no exception. With seminal work in Earth sciences published by Sander (1930) and later others (e.g. Paterson & Weiss 1961; Weiss &

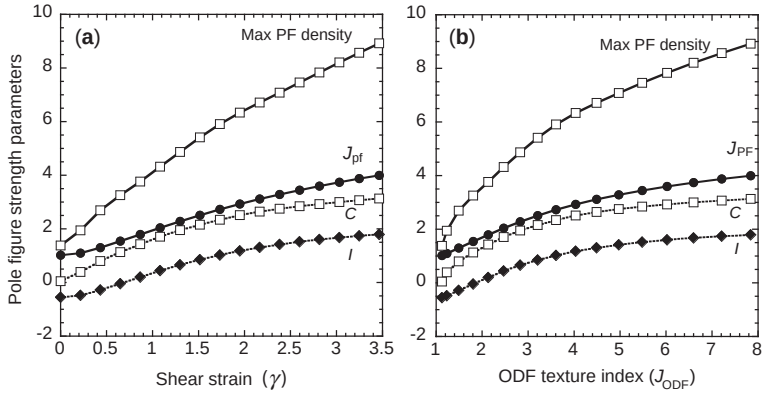

Fig. 4. Pole figure strength characteristics for olivine (100) pole figures from a VPSC simulation: (**a**) function of shear strain γ; and (**b**) function of ODF texture index J_{ODF}.

Wenk 1985; Nakamura & Nagahama 2000), these methods have remained rather conceptional than practical. Several theoretical studies have been performed (e.g. Bunge & Esling 1985; Bunge & Nielsen 1997; Bachmann *et al.* 2010), but until now they have not been widely used and quantitative analysis of ODF symmetry has in fact been quite restricted.

In Earth sciences the preoccupation has been the study of pole figures, which are well adapted for $\boldsymbol{c}$[001]-axes with a multiplicity of 1 and hence to the eigen analysis using the orientation tensor T introduced above. Various symmetry-related characteristics have been proposed using the orthogonal eigenvalues of the orientation tensor T. These include the shape characteristic $K = \ln(\lambda_1/\lambda_2)/(\ln(\lambda_2/\lambda_3)$ of Woodcock (1977) and the fabric symmetry characteristics of Vollmer (1990): point maxima $P = \lambda_1 - \lambda_2$; girdle $G = 2(\lambda_2 - \lambda_3)$; and random $R = 3\lambda_3$. These indices range from 0 to 1 and have the property that $P + G + R = 1$. Woodcock's (1977) K characteristic has values $K > 1$ for point maxima clustering and $K < 1$ for girdles. Vollmer's characteristics P, G and R have proved popular for describing omphacite clinopyroxene pole figures (e.g. Abalos 1997; Mauler *et al.* 2001). In naturally deformed eclogites, omphacite clinopyroxene pole figures display transition from a linear fabric (L-type) with girdle (010) pole figure and the [001] pole figure a point maximum, to schistosity planar fabric (S-type) with point maximum (010) pole figure and the [001] pole figure a girdle. Ulrich & Mainprice (2005) introduced the LS-index, which has a value of 1 for the end-member L-type and a value of 0 for the end-member S-type omphacite CPO

$$\mathrm{LS} = \frac{1}{2}\left[2 - \left(\frac{P_{010}}{G_{010} + P_{010}}\right) - \left(\frac{G_{001}}{G_{001} + P_{001}}\right)\right]$$

where the subscripts of the P and G indices refer to the pole figures (010) and [001]. The main idea behind a CPO symmetry index, like the LS-index of Ulrich & Mainprice (2005), is based on the fact you can use two pole figures of orthogonal crystallographic directions or axes to characterize the symmetry of the CPO in the ideal case of axial CPO (or fibre texture ODF as it is referred to in materials science). An axial CPO has one axial symmetry crystallographic direction or axis ($\boldsymbol{h}$, e.g. defined in `MTEX` as $h =$ Miller(1, 0, 0, CS, 'Olivine', 'hkl')) with specimen coordinates ($\boldsymbol{r}$, e.g. defined as $r =$ vector3d('polar', polarangle, azimuthangle)) which in `MTEX` can be used to define a fibre texture ODF with the command fibreODF(h, r, CS, SS). The axial crystallographic direction or axis will have a point maximum pole figure and all other pole figures will have either large or small circle girdles. Axial symmetries are common in specimens experimentally deformed in axial compression (e.g. Nicolas *et al.* 1973). We take as an example a common axial CPO in olivine with orthorhombic crystal symmetry so that $\boldsymbol{a}$[100], $\boldsymbol{b}$[010] and $\boldsymbol{c}$[001] are perpendicular, an axial CPO with [010] as the axial symmetry direction which will have a point maximum [010] pole figure, and [100] and [001] pole figures which will have great circle girdles normal to the [010] point maximum. In this case we can define an index based on the pole figure of the axial direction $\pm$[010] and any perpendicular direction [$u0w$]. The choice of the perpendicular direction [$u0w$] can be guided by the knowledge of one of these [$u0w$] also forms an axial direction in other specimens; in the case of olivine [100] it can also be an axial direction as shown by simple shear experiments (e.g. Bystricky *et al.* 2000). For example, we can define the BA-index as:

$$BA = \frac{1}{2}\left[2 - \left(\frac{P_{010}}{G_{010} + P_{010}}\right) - \left(\frac{G_{100}}{G_{100} + P_{100}}\right)\right]$$

where the subscripts of the P and G indices refer to the pole figures [010] or [100]. Note that for real data, Ulrich & Mainprice (2005) found that the random characteristic R of Vollmer (1990) was never zero. The P_{010} and G_{100} values are therefore normalized by the sum of $G_{010} + P_{010}$ and $G_{100} + P_{100}$, respectively, to give the desired range of 0–1 for any value of R. When the BA-index is 0 the [010] pole figure is a perfect point maximum with $P_{010} = 1$ and $\mathrm{G}_{010} = 0$ and the [100] pole figure is a perfect great circle girdle with $P_{100} = 0$ and $G_{010} = 1$. When BA-index is 1 the [010] pole figure is a great circle girdle with $P_{010} = 0$ and $G_{010} = 1$ and the [100] pole figure is a perfect point maximum with $P_{100} = 1$ and $G_{010} = 0$. When BA-index is 0.5 the [010] pole figure is a perfect point maximum with $P_{010} = 1$ and $G_{010} = 0$ and the [100] pole figure is a perfect point maximum with $P_{100} = 1$ and $G_{010} = 0$. This is the most common CPO for olivine, with all 3 pole figures [100], [010] and [001] having a point maximum. Three common olivine CPOs can be characterized by this simple BA-index using [010] and [100] pole figures; for olivine other combinations are possible (BC and AC). Note that this method based on eigenvalues does not require knowledge of the orientation of the specimen reference frame in absolute terms, for example a xenolith with no structural reference frame. When plotting results in `MTEX`, the specimen X can be defined to be north or east and the eigenvalue analysis will give the

same results; only the eigenvectors will change orientation. The eigenvalues are of course invariant with respect to rotation.

To illustrate the properties of the BA-index and the K shape factor we will use the olivine VPSC A-type CPO simulation depicted in Figures 1 and 5. The BA index and K for (100), (010) and (001) pole figures have a value 0.68, 2.40, 0.46 and 0.86, respectively, in our nearly uniform starting CPO. BA-index decreases with increasing shear strain, reaching a value of 0.50 indicative of perfect point maxima in the (100) and (010) pole figures at a shear strain of 2.81 (Fig. 5a). K for the (100) pole figure has a similar evolution to the BA-index, reaching an almost constant value of 0.65 at a shear strain of 1.52 with $K < 1$, both parameters classifying it as a girdle (Fig. 5b). This is also the case for K for (010) with $K < 1$ with value 0.65 at a shear strain of 1.73. The K for (001) varies considerably at low strain with $K < 1$ and K up to 14 at high shear strain. The value for most of the strain history is $K > 1$, indicating point maxima clustering or point maxima. The pole figures for the largest shear strain of 3.46 show all strong point maximum symmetry (Fig. 5c) with a slight tail of a girdle with very low densities for (100) and (001). The BA-index of 0.5 indicates point maxima pole figures as observed and the K characteristic for (100) and (001) $K < 1$ indicates girdles, which at most is a minor component of these pole figures. The K characteristic for the relatively weaker (001) pole figure with $K > 1$ indicates a point maxima as observed. The contoured pole figures of the VPSC model at the highest strain (Fig. 5c) shows the point maxima is well developed in all three pole figures. The individual orientation distributions are shown in Figure 1 for selected shear strain values. Note that the eigenvectors have a stable direction with respect to the density distributions at low-strain levels for (100) and (010) pole figures. The eigenvectors E1 and E3 track the high and low densities that rotate in simple shear deformation, respectively. Based on this test of the BA-index and other tests on the LS-index by Ulrich & Mainprice (2005) for axial tension, axial extension, pure shear and simple shear, it appears that normalized symmetry indices such as the LS- or BA-index correctly characterize the pole figure symmetry. In contrast, the K characteristic seems to be strongly influenced by the weaker densities in the pole figures and may give unreliable results. This is probably due to the fact it is not a normalized characteristic, and hence does not have a fixed range.

We present a brief example of the application of the BA index to a CPO transition in olivine, using data from the study of the crust–mantle transition zone of the Oman Ophiolite (Higgie & Tommasi 2012) presented earlier. The axial (010) CPO is associated with melt-rich layers, where the axial (100) CPO occurs in layers with plastic deformation microstructure. The authors used the conventional P, G and R characteristics of Vollmer (1990), but the scatter in the data from a study with all EBSD samples failed to provide a clear classification of the CPO symmetry, for example using the ODF

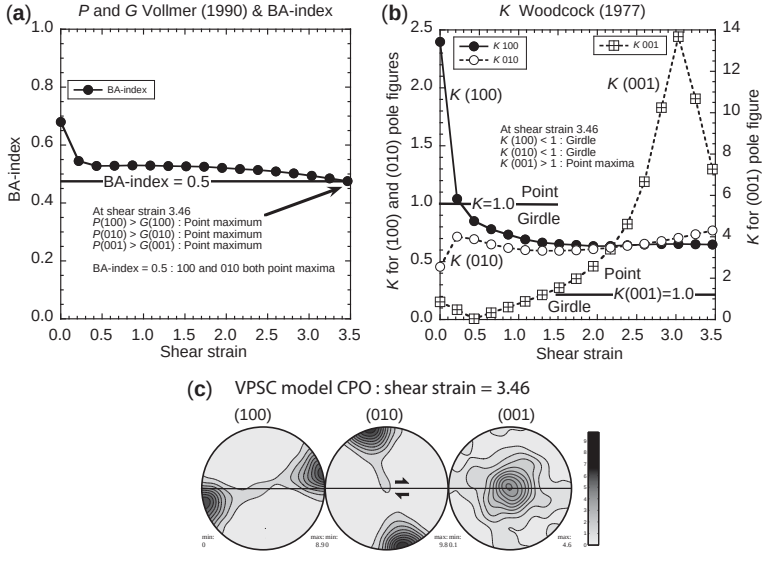

Fig. 5. Pole figure symmetry characteristics for olivine from a VPSC simulation.

texture index in Figure 6a. Using the normalization of the BA index given above it is possible to classify the 57 CPOs in a reasonable order (Fig. 6b). The data points are widely scattered, but trend lines that are linear least-squared fits to the texture indices of the ODFs and pole figures show the ODF texture index is not correlated with symmetry in Figures 6a and 6b, increasing slightly toward the axial (100) pole (BA = 1). Each pole figure has a different evolution from the axial (010) to axial (100) poles; the (100) increases, the (010) decreases and (001) is constant. Globally the (010) has the largest texture index, the (100) is intermediate and (001) has the smallest. The majority of the samples have a BA index of between 0.15 and 0.45 (Fig. 6) and there are none in the region 0.0–0.15, so a perfect axial (010) CPO dos not exist in this sample set. In contrast, there are high values of BA index up to 0.94, very close to being perfect axial (100) fabrics, as in the simple shear experiments of Bystricky *et al.* (2000).

Bingham statistics are well known in Earth sciences as a means of describing the dispersion of palaeomagnetic directions with antipodal symmetry on a sphere (Bingham 1974). The Bingham method is based on using eigenvectors of the orientation tensor used above, more commonly called the covariance matrix in statistics. Schaeben (1996), Kunze & Schaeben (2004) and Bachmann *et al.* (2010) extended the Bingham method to the distribution of quaternions. In this section we provide a brief description (more details are given in the papers cited above). Quaternions look like vectors with four coefficients, and differ from vectors in the way their multiplication is implemented. They also instructively describe a rotation in terms of its angle and axis, in a similar way to three Euler angles. A rotation can be described by a unit quaternion and is given as

$$q = \cos\frac{\omega}{2} + \boldsymbol{n}\sin\frac{\omega}{2}$$

by Meister & Schaeben (2005), where $\boldsymbol{n}$ is a Cartesian unit vector rotation axis and the angle ω is an anticlockwise rotation about $\boldsymbol{n}$. Parameterized in terms of quaternions, the obvious ODF manifold is the unit sphere in $\mathbb{R}^4$ or a torus defined by the spherical coordinates of $\boldsymbol{n}$ and the angle ω.

The important summary statistic for the Bingham quaternion distribution is the (4×4) orientation tensor T

$$T = \frac{1}{n}\sum_{l=1}^{n} q_l q_l^T,$$

where q_l is a quaternion and q_l^T is its transpose. It is sufficient to estimate its four location and four shape parameters, which can be interpreted in terms of principal axes and corresponding principal moments of inertia of a cloud of unit axes in four-dimensional real space restricted to the three-dimensional unit sphere. It should be noted that q and $-q$ describe the same rotation. The spectral decomposition of T provides the four eigenvectors (as four orthonormal quaternions) $a_1, \ldots, a_4$ and a corresponding set of real eigenvalues $\lambda_1, \ldots, \lambda_4$.

The eigenvectors immediately provide estimators of the location parameters while the eigenvalues provide estimators of the shape parameters by a system of algebraic equations involving the normalizing constant. The eigenvalues sum to 1 and are usually sorted according to some convention. The shape parameters are only determined up to an additive constant and sorted correspondingly. The Bingham quaternion distribution is antipodally symmetric and includes a bimodal bipolar case, a

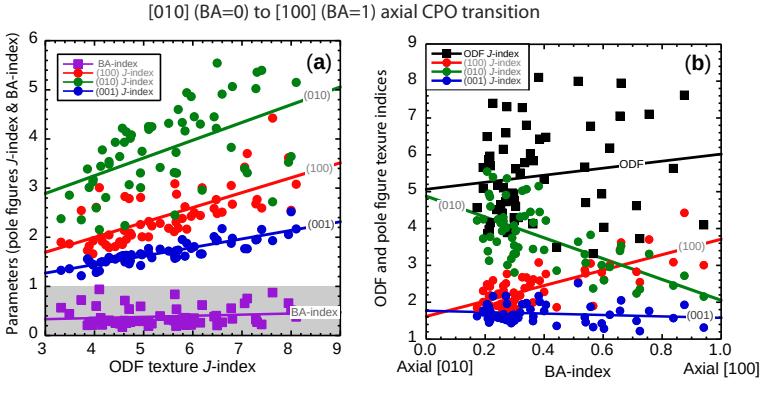

Fig. 6. Application of BA-index to the study of a CPO transition in the Oman Ophiolite. (**a**) BA-index and pole figure texture indices v. ODF texure index. (**b**) ODF and pole figure texture indices v. BA-index. The grey area in (a) is the 0–1 range of BA-index. Lines are linear least-square fits. Data from Higgie & Tommasi (2012).

multimodal great circle (fibre) case and a multimodal spherical case. Kunze & Schaeben (2004) introduced instructive parameters referring to these cases in terms of ratios of differences of shape parameters or ratios of eigenvalues, respectively. Generally, the shape of a Bingham distribution cannot be inferred from a single shape parameter or a single eigenvalue; it requires all four of them to be defined.

The Bingham quaternion distribution cannot simply be generalized to account for crystal symmetry; its symmetrization by superposition is no longer an exponential distribution and cannot generally be applied to EBSD data. For the analysis of EBSD data there is a special case of interest if the largest eigenvalue λ_1 is almost 1 or at least much bigger than the other three (e.g. $\lambda_4 \leq \lambda_3 \leq \lambda_2 \ll \lambda_1$). By sorting the individual orientation measurements such that they finally belong to one asymmetric unit of the orientation manifold, they form a highly concentrated cloud of orientations and the Bingham parameters can be estimated whatever the crystal symmetry. In this special case, λ_1 provides a measure of spherical dispersion and λ_2, λ_3, λ_4 further distinguish the shape of the highly concentrated distribution in the ODF manifold. Defining a shape factor as

$$\mathrm{SF} = \frac{\lambda_2/\lambda_3}{\lambda_3/\lambda_4},$$

it has three critical values of interest: (1) for a cloud of concentric spheres of equal density $\mathrm{SF} = 1$; (2) for an elongated cloud of cigar-like shapes (prolate) of equal density $\mathrm{SF} > 1$; and (3) for a flattened cloud of discus-like shape (oblate) of equal density $\mathrm{SF} < 1$. Details including significance tests are given by Bachmann *et al.* (2010).

In conclusion, with the limited number of parameters complex ODFs cannot be represented with Bingham methods, although ODFs with simple symmetries such as fibre and unimodal can be reasonably well approximated.

With MTEX there are two routes for making a Bingham analysis and constructing a Bingham ODF: (1) using single orientation data such as quaternions, Euler angle triplets or EBSD data; or (2) using an ODF constructed from any data type, including pole figure inversion. The second route is more universal and has the advantage of producing a continuous distribution function that has a degree of smoothness, which is more like the simple symmetries that a Bingham ODF can represent. The essential steps of the second route are as follows:

(1) determine the mean orientation (q_m), the orientation tensor (T) and eigenvalues of the ODF using the command 'mean';
(2) estimate the shape parameters κ of the Bingham quaternion distribution using the command 'evalkappa';
(3) calculate the Bingham ODF using the command 'BinghamODF';
(4) measure the error difference between your data ODF and the Bingham model ODF using the command 'calcError'; and lastly
(5) calculate the shape factor (SF) from the eigenvalues (see example script in Appendix VII).

As an example we computed the spherical dispersion (SD) and shape factor (SF) for the 1998 Olivine CPO database shown in Figure 7. The plot of spherical dispersion v. shape factor exhibits a clustering of points near the spherical shape with SF near 1. The spherical disperion values cluster around low values consistent with a strong CPO. The histogram of shape factor confirms the strong clustering around 1 with over 25% of the database near 1. The second histogram of the L1 norm error between data and model Bingham ODFs shows low values of L1 indicating a good approximation (e.g. L1 $\leq$ 0.4 are not very common).

Components

ODF modes

MTEX provides a means for detecting maxima inside an ODF, which is particularly well adapted to ODFs with a complex distribution. The command to search the ODF stored as a 3D grid for maxima has the syntax [modes, values] = calcModes(odf, n), where n is the number of maxima to be found, modes are the orientations and values are ODF densities at each orientation. An example script and output is given in Appendix VIII.

Once the modes have been detected they can be displayed using the annotate command on an ODF or pole figure plots, for example using annotate (modes, 'Marker', 's','MarkerSize', 12, 'MarkerFaceColor', 'black') after the plotodf or plotpdf commands. By using the percentage of the maximum ODF density we can constrain all the maxima to be within a specific range such as $\geq$50%. We first applied the method to the VPSC model, which shows a decrease in the number of modes with increasing shear strain (Fig. 8a). We have also searched all the 110 ODFs of the 1998 Olivine database for 5 maxima $\geq$50% and the results are shown in Figure 8b. There is clear tendency for the ODFs with low texture indices to have many maxima and the ODFs with strongest texture index to have only one, i.e. unimodal ODFs with a spherical shape and low spherical dispersion in Figure 7. The database shows the general features as the VPSC model despite the considerable scatter; this

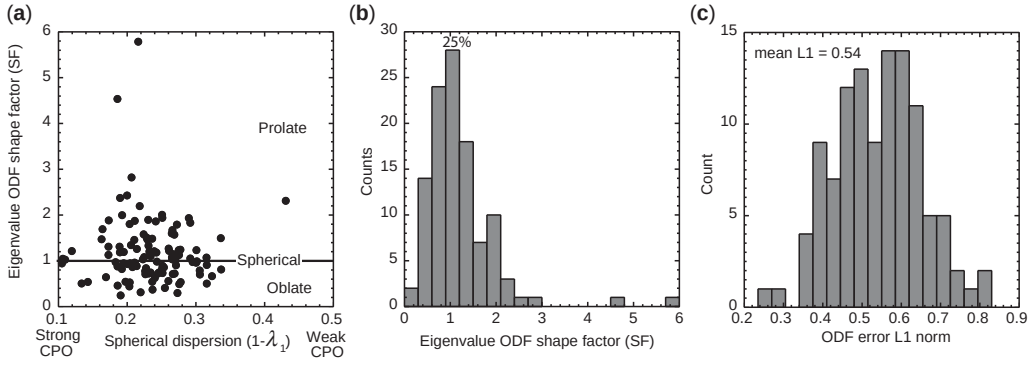

Fig. 7. Application of the Bingham method to the 1998 Olivine database: (**a**) plot of shape factor v. spherical dispersion with the field of prolate, spherical and oblate ODF shapes; (**b**) histogram of shape factor; and (**c**) histogram of L1 norm error between data and Bingham model ODFs. Data from Ben Ismaïl & Mainprice (1998).

is due to the database containing a majority of A-type CPOs.

ODF components

The components of an ODF are explicitly shown when the ODF is created or when requested using the command display(odf), which gives a standard output of crystal and specimen symmetry, the type of ODF (uniform, fibre, Bingham and radially symmetric) and other details. Some of these characteristics can be deduced using the methods given above. The construction of ODF requires specification of a radially symmetric kernel function, its half-width and/or its spherical harmonic bandwidth. Each kernel function has it advantages and disadvantages; the recommended kernel for texture work in `MTEX` is the de la Vallee Poussin. We have used de la Vallee Poussin kernel with a half-width of 10° corresponding to a bandwidth of 28 for all examples in this paper to make the presentation as homogeneous as possible. Changing the kernel function or its characteristics half-width or bandwidth will of course change the results, and this applies to this section.

Hielscher *et al.* (2006) studied the relationship between the entropy of the ODF and its texture index. During the course of this study they discovered the following relationship between entropy (S), texture index (J) and $f_{\min}$:

$$S \geq -\frac{(J-1)f_{\min}}{J-1+(1-f_{\min})^2}\ln f_{\min} - \frac{(J-f_{\min})(1-f_{\min})}{J-1+(1-f_{\min})^2}\ln\frac{(J-f_{\min})}{(1-f_{\min})}$$

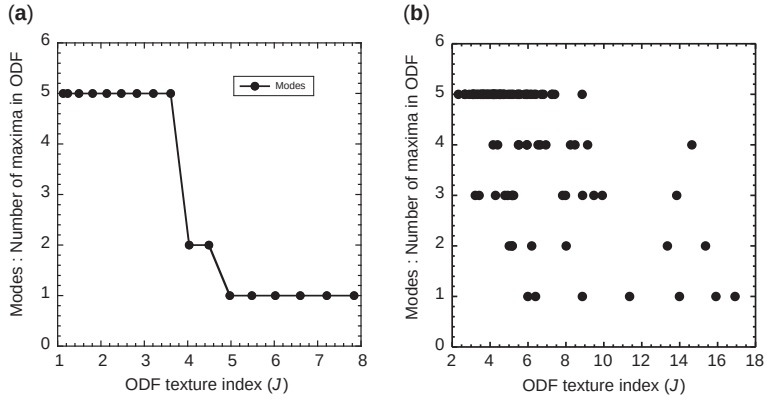

Fig. 8. Application of the calcModes to the VPSC olivine simple shear model and 1998 olivine database. Two plots of number of modes with ODF densities ≥50% of the maximum density v. ODF texture index: (**a**) VPSC olivine simple shear model; and (**b**) 1998 olivine database. Data from Ben Ismaïl & Mainprice (1998).

and, in particular, $0 \geqslant S \geqslant -\ln J$ where $f_{\min}$ is the lower bound of the uniform component of the ODF. For any pair of values for S and J the value of $f_{\min}$ can be found by iteration, except for the trivial case of uniform ODF where $S = 0$, $J = 1$ and $f_{\min} = 1$. To understand how $f_{\min}$ varies with uniform ODF component, we have constructed a simple linear mixing model with the code modelODF = Xf × uniformODF + (1 − Xf) × unimodalODF, where Xf is volume fraction of uniform ODF component. The method is illustrated in the example script in Appendix IX.

We have calculated $f_{\min}$ as a function of the ODF texture index (Fig. 9a). The $f_{\min}$ fraction progessively decreases, as expected, with increasing ODF texture index. The $f_{\min}$ fraction reaches a nearly constant low value at ODF texture index of about 4. The calculation of $f_{\min}$ for the olivine 1998 CPO database shows high values at low ODF texture index and increasingly lower values at higher texture index (Fig. 9b), although there is considerable scatter.

Elastic tensor symmetry components

In seismology the heterogeneous distribution of earthquake sources (e.g. subduction zones and faults) and receivers (e.g. seismometers), as well as the complexity of inversion methods, justifies undertaking anisotropy analysis assuming a high-elastic symmetry within the Earth to reduce the number of independent coefficients. The most frequently used assumption is to use hexagonal (also called transverse isotropy in geophysics) with only five independent coefficients. To understand the impact of high-elastic symmetry in seismological analysis has been the motivation for geophysical interest in the decomposition of a general triclinic elastic tensor into components of higher symmetry (e.g. Backus 1970; Harder 1988; Arts *et al.* 1991; Mainprice & Silver 1993; Browaeys & Chevrot 2004). We have implemented the method of Browaeys & Chevrot (2004) which is based on the Euclidean norm of a general triclinic elastic tensor. The Euclidean norm is defined in the standard way by $\sqrt{X \cdot X}$ where X is a Euclidean vector with 21 elements, filled with 21 independent coefficients of the elastic tensor in the form of an eigentensor (Kelvin 1856). The transformation of a Voigt elastic stiffness tensor $C(i, j)$ to Euclidean vector X is

$$X = [C(1,1), C(2,2), C(3,3), \sqrt{2}C(2,3), \sqrt{2}C(1,3), \sqrt{2}C(1,2), C(4,4), C(5,5), C(6,6), 2C(1,4), 2C(2,5), 2C(3,6), 2C(3,4), 2C(1,5), 2C(2,6), 2C(2,4), 2(3,5), 2C(1,6), 2\sqrt{2}C(5,6), 2\sqrt{2}C(4,6), 2\sqrt{2}C(4,5)]^{\boldsymbol{T}}.$$

The general triclinic Euclidean vector X can be be decomposed into a series of vectors representing each symmetry class to be analysed such as the holohedral elastic classes (triclinic, monoclinic, orthorhombic, tetragonal, hexagonal and isotropic):

$$X = X_{\text{tric}} + X_{\text{mono}} + X_{\text{ortho}} + X_{\text{tetra}} + X_{\text{hex}} + X_{\text{iso}}$$

with 21, 13, 9, 6, 5 and 2 independent constants, respectively. The Euclidean norm is used as a distance function measuring the difference between, for example, a monoclinic and a higher symmetry orthorhombic tensor,

$$D_{\text{mono}} = \sqrt{X - X_{\text{mono}}} \cdot \sqrt{X - X_{\text{mono}}},$$

$$D_{\text{ortho}} = \sqrt{X - X_{\text{ortho}}} \cdot \sqrt{X - X_{\text{ortho}}},$$

$$P_{\text{mono-ortho}} = 100(D_{\text{ortho}} - D_{\text{mono}})/\sqrt{X \cdot X},$$

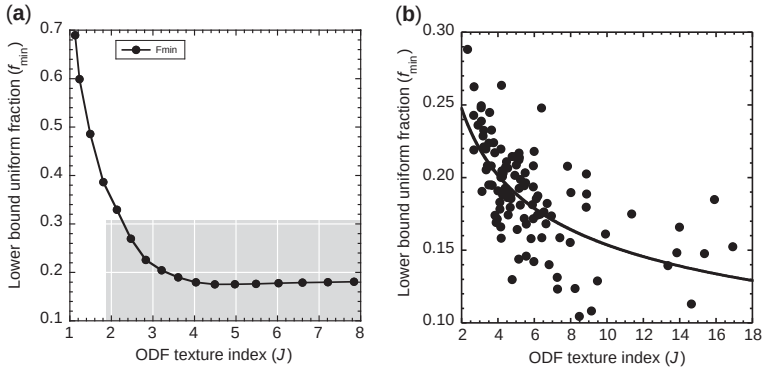

Fig. 9. Application of the $f_{\min}$ lower bound of the uniform component of the ODF v. ODF texture index: (**a**) olivine VPSC simple shear model; and (**b**) olivine 1998 CPO database. A half-width of 10° was used for all the ODF calculations. The grey area in (a) corresponds to the data range in (b).The trend line in (b) is a power law fit to the data (no physical meaning is attached to this fit). Data from Ben Ismaïl & Mainprice (1998).

where the Euclidean vector of the arbitrary tensor $C(i,j)$ to be analysed is X and the Euclidean vectors of the tensors for monoclinic and orthorhombic components are X_{mono} and X_{ortho}, respectively, which have been constructed from X using the method of orthogonal projectors. $P_{\text{mono}-\text{ortho}}$ is the percentage contribution of the component of the monoclinic symmetry class in the interval from monoclinic to orthorhombic. Further computational details of the construction of the symmetry classes using projectors are given in the appendix of Browaeys & Chevrot (2004).

Although the Euclidean norm is the obvious choice, it is not invariant under inversion of the elastic tensor and different values are obtained when using stiffness and compliance tensors (Moakher & Norris 2006). It is therefore recommended to use Browaeys & Chevrot (2004) analysis only when using the Voigt stiffness tensor, for example as calculated from polycrystalline aggregate using the Voigt average. Moakher & Norris (2006) discuss other norms suitable for the stiffness and compliance tensors.

As an example we can apply this method to the olivine CPO database of Ben Ismaïl & Mainprice (1998). The following steps are required for all 110 CPOs:

(1) import CPO into `MTEX` using the command loadEBSD;
(2) calculate ODF using calcODF;
(3) calculate the elastic stiffness tensors with calcTensor; and finally
(4) convert tensor to matrix form and decomposition of the elastic tensor using the `Elastic_Tensor_Decomposition` (see example script in Appendix X).

We applied the method to our VPSC model and plotted the results as function of ODF texture index in Figure 10a. We find that our initial random CPO results in an isotropic tensor, as expected, with no anisotropic components. The anisotropic elastic components with monoclinic and orthorhombic symmetry increase rapidly with ODF texture index, whereas all other anisotropic components are close to zero. As simple shear strain has monoclinic macro-scale symmetry, it is perhaps not surprising that the monoclinic elastic component is dominant in the VPSC model. The orthorhombic component is clearly associated with the development of the A-type CPO, which has macro-scale orthorhombic symmetry related to the CPO with point maxima of (100), (010) and (001). Results of the application of the method to the olivine database is plotted in Figure 10b as mean values for each symmetry class displayed as a histogram. The orthorhombic symmetry has the highest frequency of 3.6% in 1998 CPO database. The most common CPO in the database is A-type, which seems to correlate well with results from the VPSC model. To put these anisotropic results from the database into perspective, the dominant elastic symmetry component (not in histogram) is an isotropic component with frequency of 91.7% for the database. Elastic anisotropy is therefore a small component when compared to isotropic anisotropy.

Conclusions

We have illustrated the use of `MTEX` commands for the evaluation of strength, symmetry and components of textures. Many of these commands can be applied to the ODF or uncorrelated MDF, and

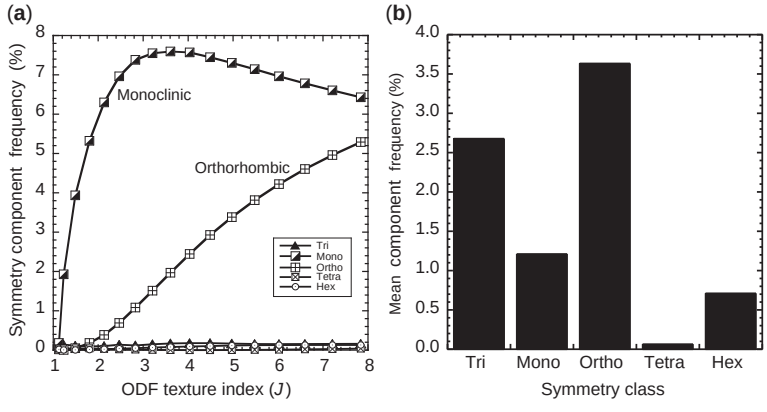

Fig. 10. (**a**) Plot of elastic symmetry components frequency v. ODF texture index for the olivine simple shear model. (**b**) Histogram of the mean frequency for the anisotropic elastic components for the 110 samples of the olivine CPO database of Ben Ismaïl & Mainprice (1998). Note that the dominant isotropic elastic components (*c.* 90%) are excluded from these figures to allow the variation of the anisotropic components to be seen.

hence can be universally applied to these density functions calculated from single orientation or inversion of pole figure data. The traditional methods of characterizing texture strength are all of the form $\| f \|^2_{L^2}$, including J_{ODF}, J_{MDF} and J_{PF}. They are sensitive to high values and are integrals of density functions, which are probabilities. In contrast, the entropy S of an ODF is sensitive to low values and hence very complimentary to J_{ODF}. The M-index has been formulated as a measure of uncorrelated MDF here and is L^1-norm of the difference of uniform and measured probability density functions. It measures the probability mass that is differently distributed, which is clearly very different to the traditional parameters. All these parameters are influenced by crystal and specimen symmetry for ODF and crystal symmetry for MDF. In addition, pole figures J_{PF} are strongly influenced by the crystallographic multiplicity of the plane normal or direction such that any analysis using J_{PF} must take this into account. Other measures of texture strength can be derived from eigen analysis of pole figures or ODFs. In principle, the eigen analysis can only be applied in the absence of symmetry. It therefore has to be applied with caution and in restricted conditions, such as antipodal symmetry or very strong and simple CPO-like fibre textures. On the other hand, eigen analysis provides a measure of 'simplified' symmetry for pole figures and ODFs of spherical, prolate or oblate shapes of their distributions. Two types of components of the ODF can be determined: (1) maxima of the ODF, which provide convenient method for defining modes; and (2) lower bounds of the uniform component of the ODF (f_{min}), providing a value of non-orientated fraction that may have applications in some physical processes e.g. recrystallization and phase transformation. Finally, we also implemented the decomposition of arbitrary elastic tensors into symmetry components, which is useful in global geophysics.

It is pleasure for DM to dedicate this paper to Professor E. Rutter who introduced him to crystal-preferred orientation, and many other things, as part of his Masters course at Imperial College London. DM thanks J. Mecklenburgh for help in translating his FORTRAN routine for the pole figure texture index and S. Chevrot for providing his FORTRAN code for the decomposition of the elastic tensor. The authors thank both reviewers for their pertinant and constructive remarks, which significantly improved the presentation. We give a special mention of thanks to E. Mariani for her editorial assistance and for making this special volume possible. This contribution is a result of scientific cooperation on the research project 'Texture and Physical Properties of Rocks', funded by the French–German program EGIDE-PROCOPE. This bilateral program is sponsored by the German Academic Exchange Service (DAAD) with financial funds from the federal ministry of education and research (BMBF) and the French ministry of foreign affairs.

Appendix I Script and output: specification of ODF

Script

```
myODF = unimodalODF(orientation('Euler', 10*
  degree, 20*degree, 30*degree), ...
symmetry('mmm'), 'halfwidth', 10*degree)
```

Output

```
myODF = ODF (show methods, plot)
crystal symmetry: mmm
sample symmetry : triclinic
Radially symmetric portion:
    kernel: de la Vallee Poussin, hw = 10
    center: (10,20,30)
    weight: 1
```

Appendix II Script and output: ODF texture index

Script

```
% Olivine crystal symmetry
CS = symmetry ('mmm', [4.756  10.207  5.98],
  'mineral', 'Olivine')
% specimen symmetry
SS = symmetry ('-1')
% Olivine orientation g
g = orientation ('Euler', 0*degree, 0*degree,
  0*degree, CS, SS)
Olivine_ODF_single_crystal = unimodalODF
  (g, 'halfwidth', 10*degree)
J_Olivine = textureindex (Olivine_ODF_single_
    crystal)
% Plagiocase An80 crystal symmetry
CS = symmetry('-1', [8.178  12.87  14.187],
  [93.5, 115.9, 90.65]*degree,...
  'X||a*', 'Z||c', 'mineral', 'An80');
% Plagiocase An80 orientation g
g = orientation('Euler', 0*degree, 0*degree,
  0*degree, CS, SS)
AN80_ODF_single_crystal = unimodalODF
  (g, 'halfwidth', 10*degree)
J_AN80 = textureindex (AN80_ODF_single_crystal)
% ratio triclinic AN80 to orthorhombic
  Olivine J_AN80/J_Olivine
Ratio = J_AN80/J_Olivine
```

Output

```
g = orientation (show methods, plot)
  size: 1 x 1
  crystal symmetry: Olivine (mmm)
  sample symmetry : -1
  Bunge Euler angles in degree
  phi1 Phi phi2
    0    0    0
Olivine_ODF_single_crystal = ODF
  (show methods, plot)
  crystal symmetry: Olivine (mmm)
  sample symmetry : -1
  Radially symmetric portion:
    kernel: de la Vallee Poussin, hw = 10
    center: (0,0,0)
    weight: 1
```

```
J_Olivine = 140.0125
g = orientation (show methods, plot)
  size: 1 x 1
  crystal symmetry: An80 (-1, X||a*, Z||c)
  sample symmetry : -1
  Bunge Euler angles in degree
  phi1 Phi phi2
    0    0    0
AN80_ODF_single_crystal = ODF (show methods, plot)
  crystal symmetry: An80 (-1, X||a*, Z||c)
  sample symmetry : -1
  Radially symmetric portion:
    kernel: de la Vallee Poussin, hw = 10Â°
    center: (0, 0, 0)
    weight: 1
    J_AN80 = 560.0500
    Ratio = 4.0000
```

Appendix III Script and output: MDF texture index

Script

```
% Olivine crystal symmetry
CS = symmetry ('mmm', [4.756 10.207 5.98],
  'mineral', 'Olivine');
% Olivine orientation g1
g1 = orientation ('Euler', 0*degree, 0*degree,
  0*degree, CS, SS);
Olivine_odf_g1 = unimodalODF (g1, 'halfwidth',
  10*degree);
% Olivine orientation g2
g2 = orientation ('Euler', 0*degree, 90*degree,
  0*degree, CS, SS);
Olivine_odf_g2 = unimodalODF (g2, 'halfwidth',
  10*degree);
% uncorrelated Misorientation Distribution
  Function
mdf_uncorrelated = calcMDF (Olivine_odf_g2,
  Olivine_odf_g1,...
  'uncorrelated', 'halfwidth', 10*degree)
% texture index for MDF
J_MDF_olivine = textureindex (mdf_uncorrelated)
% Plagiocase An80 crystal symmetry
CS = symmetry ('-1', [8.178  12.87  14.187],
  [93.5, 115.9, 90.65] * degree ,...
'X||a*', 'Z||c', 'mineral', 'An80');
% Plagiocase An80 orientation g1
g1 = orientation ('Euler', 0*degree, 0*degree,
  0*degree, CS, SS);
AN80_odf_g1 = unimodalODF(g1,'halfwidth',
  10*degree);
% Plagiocase An80 orientation g2
g2 = orientation ('Euler', 0*degree, 90*egree,
  0*degree, CS, SS);
AN80_odf_g2 = unimodalODF (g2, 'halfwidth',
  10*degree);
% uncorrelated Misorientation Distribution
  Function
mdf_uncorrelated = calcMDF (AN80_odf_g1,
  AN80_odf_g2, ...
  'uncorrelated', 'halfwidth', 10*degree)
% texture index for MDF
J_MDF_AN80 = textureindex (mdf_uncorrelated)
% ratio
Ratio = J_MDF_AN80/J_MDF_olivine
```

Output

```
mdf_uncorrelated = MDF (show methods, plot)
  crystal symmetry: Olivine (mmm)
  crystal symmetry: Olivine (mmm)
  Portion specified by Fourier coefficients:
    degree: 28
    weight: 1
J_MDF_olivine = 50.4447
mdf_uncorrelated = MDF (show methods, plot)
  crystal symmetry: An80 (-1, X||a*, Z||c)
  crystal symmetry: An80 (-1, X||a*, Z||c)
  Portion specified by Fourier coefficients:
    degree: 28
    weight: 1
J_MDF_AN80 = 201.7788
Ratio = 4.00
```

Appendix IV Script: M-index

Script

```
% Step 1 : Uniform misorientation angle
  distribution
% Define Crystal symmetry (should match with
  your data)
CS_Orthorhombic = symmetry ('mmm');
% get the misorientation angle distribution for
  crystal symmetry mmm
[density_uniform,~] = angleDistribution
  (CS_Orthorhombic);
% normalize the misorientation angle
  distribution
density_uniform = density_uniform/sum
  (density_uniform);
% Step 2 : calculate the uncorrelated MDF
  from ODF
% Calculate uncorrelated MDF from ODF
MDF = calcMDF(ODF);
% Step 3 : uncorrelated misorientation angle
  distribution from MDF
[density_MDF,~] = calcAngleDistribution (MDF,
'resolution', 1*degree);
% normalize the misorientation angle
  distribution
density_MDF = density_MDF/sum(density_MDF);
% Step 4 : calculate the M-index
M_index = (sum((abs(density_uniform-density_
  MDF))/2));
```

Appendix V Script and output: pole figure texture index and multiplicity for quartz

Script

```
% J_pf example alpha-quartz
% crystal symmetry and Euler angle frame
CS = symmetry('-3m', [4.916  4.916  5.4054],
  'X || a*', 'Z||c', ...
  'mineral', 'alpha-quartz');
% triclinic specimen symmetry
SS = symmetry('-1');
% orientation g
g = orientation ('Euler', 0*degree, 0*degree,
  0*degree, CS, SS);
Quartz_ODF = unimodalODF (g, 'halfwidth',
  10*degree);
% Classic Quartz selection of pole figures (hkil)
% c(0001), a(2-1-10), m(10-10), r(10-11), z(1-101)
h = [Miller(0, 0, 0, 1, CS, 'hkl'), Miller (2, -1,
  -1, 0, CS, 'hkl'), ...
```

```
Miller (1,0, -1, 0, CS, 'hkl'), Miller
  (1, 0, -1, 1, CS, 'hkl'), ...
Miller (1, -1, 0, 1, CS, 'hkl')];
% number of pole figures
no_pfs = length (h);
% Pole figure grid (r) and volume increment dr
% 1 degree pole figure grid
resolution = 1;
r = S2Grid ('regular', 'resolution', resolution
  *degree);
% get polar angle theta of pole figure grid
[theta] = polar (r);
% normalize by 4*pi for grid on sphere (upper and
  lower hemispheres)
dr = (resolution.*degree).^2.*cos (resolution
  *degree)./4./pi;
% calculate pole figure density on 1 degree grid
pfs = calcPoleFigure (Quartz_ODF, h, r,
  'complete');
% plot pole figures
plotpdf (Quartz_ODF,h)
% get maximum values of all pole figures
pfs_max (1:no_pfs) = max (pfs);
% Pole figure texture index
% preallocation memory for pole figures
pfT2 = zeros (no_pfs);
fprintf('h  k  i  l  Max  Jpf  m  m x Jpf \n')
for ipole = 1:no_pfs
% get intensities P_h(r)
  d = get (pfs(ipole), 'intensities');
  d = reshape (d,size (r));
% Normalized pole figure texture index
  pfT2(ipole) = sum (sum(dr.*sin(theta).*d.^2))/
    sum(sum(dr.*sin(theta).*d));
% multiplicity of pole figure for
% uniquely for alpha-quartz with c-axis
  multiplicity = 2
  m = 2*pfT2(1)/pfT2(ipole);
% product m x Jpf
  mJpf = m*pfT2(ipole);
% get hkil
  h = get(pfs(ipole), 'h');
  pf_hkl = get(h, 'hkl');
  fprintf('%2i %2i %2i
%2i %6.2f %6.2f %4.1f %6.2f \n',...
  pf_hkl (1,1),
  pf_hkl(1,2), pf_hkl(1,3), pf_hkl(1,4),...
  pfs_max (ipole), pfT2 (ipole), m, mJpf)
end
```

Output

h	k	I	L	Max	Jpf	m	m × Jpf
0	0	0	1	45.95	23.07	2.0	46.15
2	-1	-1	0	30.63	15.40	3.0	46.15
1	0	-1	0	15.32	7.70	6.0	46.15
1	0	-1	1	15.31	7.70	6.0	46.15
1	-1	0	1	15.31	7.70	6.0	46.15

Appendix VI Script: orientation tensor, eigenvectors and -values, and Vollmer *P* and *G* parameters for Bytownite

Script

```
% Step 1 Extract individual orientations from
  ebsd object
o = get(ebsd('BYTOWNITE'), 'orientations');
% Step 2 vectors of [100] directions in specimen
  co-ordinates
v = o * Miller(1, 0, 0, CS, 'BYTOWNITE', 'uvw');
% Step 3 extract x,y,z components from v
[x,y,z] = double(v);
% Step 4 orientation tensor OT
% OT = weighted multipication of the column
  vector by a row vector
% of the scatter data OT = 1/n ([x,y,z]T.[x,y,z])
OT = 1./numel(x)*[x,y,z]'*[x,y,z];
% Step 5 Eigen-values and -vectors of OT matrix
[Vec, Diagonal] = eig(OT);
% Step 5 Eigen-values : conversion diagonal
  matrix to vector
value = diag (Diagonal);
% Step 6 Sort Eigen-values in descending order
[value,index] = sort (value, 'descend');
% Step 7 Sort Eigen-vectors
vec1(1:3) = Vec (: ,index(1));
vec2(1:3) = Vec (: ,index(2));
vec3(1:3) = Vec (: ,index(3));
% Step 8 Calculate Vollmer (1990) P and G
  distribution parameters
NORM = value(1) + value(2) + value(3);
% Point maximum
P100 = (value(1)-value(2))/NORM
% Girdle
G100 = (2.0*(value(2)-value(3)))/NORM
```

Appendix VII Script: mean orientation, eigenvectors and -values of a classical ODF, and calculating the Bingham ODF, its spherical dispersion and shape factor

Script

```
% Bingham analysis and Bingham ODF construction
% mean orientation qm, Eigen-values (lambda)
  and orientation tensor (T)
[qm,lambda,T] = mean(dataODF);
% kappa for Bingham ODF estimated from
  Eigen-values
kappa = evalkappa(lambda, 'approximated');
% kappa and ODF orientation tensor (T), CS and
  SS define Bingham ODF
modelODF = BinghamODF(kappa, T, CS, SS)
% measure of ODF difference data - model with
  the L1 norm
Error = calcError(dataODF, modelODF, 'L1')
% Parameters associated with eigenvalues
  (Lambda)
% sort into descending order for lambda
lambda = sort(lambda, 'descend');
% SD measure of spherical dispersion
SD = 1.0 - lambda(1);
% SF Shape factor
SF = (lambda(2)/lambda(3))/(lambda(3)/
  lambda(4))3;
```

Appendix VIII Script and output: detecting modes in an ODF

Script

```
% Calculate modes in ODF
% modes (orientations) and values (densities)
[modes, values] = calcModes(odf,n);
```

```
% number of modes dectected (n or less)
n_modes = numel(values);
% calculate percent of maxium ODF density for
  all modes
% extract Euer angles from modes
Mode_euler = get (modes, 'Euler')/degree;
% print results
fprintf('\n');
fprintf(' Number modes searched = %i \ n', n);
fprintf(' \n');
fprintf('  Detected modes \n');
fprintf(' Mode No. Percent density phi1 PHI
  phi2 \n');
for i = 1:n_modes
  percent = 100*values(i)/values(1);
  fprintf(' %i %8.2f %8.2f %8.2f %8.2f \n', i,
    percent, Mode_euler(i,:)) ;
end
```

Output

```
Number modes searched = 5
                  Detected modes
Mode    Percent     phi1      PHI      phi2
No.     density
1        100.00    104.72   77.58     8.91
2         90.37    307.60   33.77   154.94
3         74.09    293.58   62.27   161.85
4         52.47    100.47   34.13    22.41
5         34.84    156.40   53.54   164.76
```

Appendix IX Script: linear mixing law for two ODFs

Script

```
% model unimodal ODF is A-type olivine CPO
  [100](010) : a//x b//y c//z
% model uniform ODF
odf_uniform = uniformODF(CS,SS);
% Define volume fraction range for uniform
  component
Xfmin = 0.00; Xfmax = 0.99;
Range = Xfmax - Xfmin;
Steps = 100;
Delta = Range/Steps;
for II = 1:Steps
% fraction model uniform ODF
  Xf = Xfmin + II*Delta;
  VolFrac(II) = Xf;
% model unimodal ODF with half width of 2
odf_type(1,:) = Xf*odf_uniform +...
(1.0-Xf)*unimodalODF(orientation('Euler',
  0*degree,0*degree,0*degree),...
CS, SS, 'halfwidth',2*degree);
% model unimodal ODF with half width of 10
odf_type(2,:) = Xf*odf_uniform +...
(1.0-Xf)*unimodalODF(orientation('Euler',
  0*degree, 0*degree,0*degree),...
CS, SS, 'halfwidth',10*degree);
% model unimodal ODF with half width of 30
odf_type(3,:) = Xf*odf_uniform +...
(1.0-Xf)*unimodalODF(orientation('Euler',
  0*degree,0*degree,0*degree),...
CS, SS, 'halfwidth', 30*degree);
% loop over model unimodal ODF with diferent
  halfwidths for n = 1:3
% Texture index of odf (J)
  J = textureindex (odf_type(n,:));
% Entropy of odf (S)
  S = real(entropy(odf_type(n,:)));
% Lower bound uniform fraction (fmin)
  fmin(n,II) = Find_Lower_Bound_Fmin_
  ODF(J,S);
  end
end
```

Appendix X Script: analysis of the symmetry of an elastic stiffness tensor

Script

```
% Step 1
% create an EBSD variable containing the
  olivine orientation data
% as phi1, PHI, phi2 using the Bunge Euler
  convention
% and default active rotation.
ebsd = loadEBSD (file_name, CS, SS, 'interface',
  'generic',...
'ColumnNames', {'phi1' 'Phi' 'phi2'}, 'Columns',
  [1 2 3], 'Bunge');
% Step 2
% Default odf for physical properties with
  Dirichlet kernel
% with Band-width = Lmax = 4 for elastic
  properties (tensor 4th rank)
K_L4 = kernel('Dirichlet',4);
odf_d = calcODF(ebsd('Olivine'), 'kernel', K_L4);
% Step 3
% Calculate the Voigt average stiffness tensor
  using ODF and
% single crystal olivine stiffness tensor
  [C_Voigt, C_Reuss, C_Hill] = calcTensor(odf_
  d,C_Olivine_Single_Crystal);
% Step 4
% convert tensor to Voigt 6 by 6 matrix form
M_Voigt = matrix(C_Voigt,'Voigt');
% Perform elastic tensor decomposition
[Psym,Std_Error_std,Csym] = Elastic_Tensor_
  Decomposition(M_Voigt);
```

References

ABALOS, B. 1997. Omphacite fabric variation in the Cabo Ortegal eclogite (NW Spain): relationship with strain symmetry during high-pressure deformation. *Journal of Structural Geology*, **19**, 621–637.

ARTS, R. J., HELBIG, K. & RASOLOFOSAON, P. N. J. 1991. General anisotropic elastic tensors in rocks: approximation, invariants and particular directions. *61st Annual International Meeting, Society of Exploration Geophysicists*, Expanded Abstracts, ST2.4, SEG, Tulsa, 1534–1537.

BACHMANN, F., HIELSCHER, H., JUPP, P. E., PANTLEON, W., SCHAEBEN, H. & WEGERT, E. 2010. Inferential statistics of electron backscatter diffraction data from within individual crystalline grains. *Journal of Applied Crystallography*, **43**, 1338–1355.

BACHMANN, F., HIELSCHER, R. & SCHAEBEN, H. 2011. Grain detection from 2d and 3d EBSD data – Specification of the MTEX algorithm. *Ultramicroscopy*, **111**, 1720–1733.

BACKUS, G. E. 1970. A geometrical picture of anisotropic elastic tensors. *Reviews of Geophysics and Space Physics*, **8**, 633–671.

BASCOU, J., TOMMASI, A. & MAINPRICE, D. 2002. Plastic deformation and development of clinopyroxene

lattice-preferred orientation in eclogites. *Journal of Structural Geology*, **24**, 1357–1368.

Ben Ismaïl, W. & Mainprice, D. 1998. A statistical view of the strength of seismic anisotropy in the upper mantle based on petrofabric studies of Ophiolite and xenolith samples. *Tectonophysics*, **296**, 145–157.

Bingham, C. 1974. An antipodally symmetric distribution on the sphere. *Annals of Statistics*, **2**, 1201–1225.

Browaeys, J. M. & Chevrot, S. 2004. Decomposition of the elastic tensor and geophysical applications. *Geophysical Journal International*, **159**, 667–678.

Bunge, H. J. 1969. *Mathematische Methoden der Texturanalyse*. Akademie-Verlag, Berlin.

Bunge, H. J. 1982. *Texture Analysis in Materials Science: Mathematical Models*. Butterworths, London.

Bunge, H. J. & Esling, C. 1985. Symmetries in texture analysis. *Acta Crystallographica*, **A41**, 59–67.

Bunge, H. J. & Nielsen, I. 1997. Generalization of the concept of sample symmetry – fuzzy symmetry, symmetroids, similarity. *Textures and Microstructures*, **29**, 127–154.

Bystricky, M., Kunze, K., Burlini, L. & Burg, J.-P. 2000. High shear strain of olivine aggregates: rheological and seismic consequences. *Science*, **290**, 1594–1597.

Curie, P. 1894. Sur la symétrie dans les phénomènes physiques, symétrie d'un champ électrique et d'un champ magnétique. *Journal of Theoretical and Applied Physics*, **3**, 393–415.

Darot, M. & Bouchez, J. L. 1976. Study of directional data distributions from principal preferred orientation axes. *Journal of Geology*, **84**, 239–247.

Engler, O. & Randle, V. 2010. *Introduction to Texture Analysis: Macrotexture, Microtexture, and Orientation Mapping*. CRC Press, Taylor and Francis Group, Boca Raton, USA.

Fisher, R. A. 1953. Dispersion on a sphere. *Proceedings of the Royal Society of London, Series A*, **217**, 295–305.

Grimmer, H. 1979. Distribution of disorientation angles if all relative orientations of neighbouring grains are equally probable. *Scripta Metallurgica*, **13**, 161–164.

Harder, S. 1988. Analysis of elastic symmetry from velocity measurements with applications to dunite and bronzitite. *Geophysical Journal*, **94**, 469–477.

Hielscher, R. & Schaeben, H. 2008. A novel pole figure inversion method: specification of the MTEX algorithm. *Journal of Applied Crystallography*, **41**, 1024–1037, http://dx.doi.org/10.1107/S0021889808030112

Hielscher, R., Schaeben, H. & Chateigner, D. 2006. On the entropy to texture index relationship in quantitative texture analysis. *Journal of Applied Crystallography*, **40**, 371–375, http://dx.doi.org/10.1107/S0021889806055476

Higgie, K. & Tommasi, A. 2012. Feedbacks between deformation and melt distribution in the crust-mantle transition zone of the Oman ophiolite. *Earth and Planetary Science Letters*, **359–360**, 61–72, http://dx.doi.org/10.1016/j.epsl.2012.10.003

Kelvin, L. (William Thomson) 1856. Elements of a mathematical theory of elasticity, Part I, On stresses and strains. *Philosophical Transactions of the Royal Society*, **1666**, 481–498.

Kunze, K. & Schaeben, H. 2004. The Bingham distribution of quaternions and its spherical Radon transform in texture analysis. *Mathematical Geology*, **36**, 917–943.

Lebensohn, R. A. & Tomé, C. N. 1993. A self-consistent anisotropic approach for the simulation of plastic deformation and texture development of polycrystals: application to zirconion alloys. *Acta Metallurgica et Materialia*, **41**, 2611–2624.

Lisle, R. J. 1985. The use of the orientation tensor for the description and statistical testing of fabrics. *Journal of Structural Geology*, **7**, 115–117.

Mainprice, D. & Silver, P. G. 1993. Interpretation of SKS-waves using samples from the subcontinental lithosphere. *Physics of the Earth and Planetary Interiors*, **78**, 257–280.

Mainprice, D., Hielscher, R. & Schaeben, H. 2011. Calculating anisotropic physical properties from texture data using the MTEX open-source package. *In*: Prior, D. J., Rutter, E. H. & Tatham, D. J. (eds) *Deformation Mechanisms, Rheology and Tectonics: Microstructures, Mechanics and Anisotropy*. Geological Society, London, Special Publications, **360**, 175–192.

Mardia, K. V. 1972. *Statistics of Directional Data*. Academic Press, New York.

Mardia, K. V. & Jupp, P. E. 2000. *Directional Statistics*. John Wiley and Sons, Chichester, UK.

Matthies, S., Vinel, G. W. & Helming, K. 1987. *Standard Distributions in Texture Analysis Volume 1*. Akademie-Verlag, Berlin.

Mauler, A., Godard, G. & Kunze, K. 2001. Crystallographic fabrics of omphacite, rutile and quartz in Vendee eclogites (Armorican Massif, France). Consequences for deformation mechanisms and regimes. *Tectonophysics*, **342**, 81–112.

Meister, L. & Schaeben, H. 2005. A concise quaternion geometry of rotations. *Mathematical Methods in the Applied Sciences*, **28**, 101–126.

Moakher, M. & Norris, A. N. 2006. The closest elastic tensor of arbitrary symmetry to an elasticity tensor of lower symmetry. *Journal of Elasticity*, **85**, 215–263, http://dx.doi.org/10.1007/s10659-006-9082-0

Morawiec, A. 2004. *Orientations and Rotations Computations in Crystallographic Textures*. Springer, Berlin.

Nakamura, N. & Nagahama, H. 2000. Curie symmetry principle: does it constrain the analysis of structural geology? *Forma*, **15**, 87–94.

Nicolas, A., Boudier, F. & Boullier, A. M. 1973. Mechanism of flow in naturally and experimentally deformed peridotites. *American Journal of Science*, **273**, 853–876.

Paterson, M. S. & Weiss, L. E. 1961. Symmetry concepts in the structural analysis of deformed rocks. *Geological Society of America Bulletin*, **72**, 841–882.

Sander, B. 1930. *Gefügekunde der Gesteine*. Springer, Vienna.

Schaeben, H. 1988. Entropy optimization in quantitative texture analysis. *Journal of Applied Physics*, **64**, 2236–2237.

Schaeben, H. 1996. Texture approximation or texture modelling with components represented by the von Mises-Fisher matrix distribution on SO(3) and the

Bingham distribution on S4+. *Journal of Applied Crystallography*, **29**, 516–525.

SKEMER, P., KATAYAMA, I., JIANG, Z. & KARATO, S.-I. 2005. The misorientation index: development of a new method for calculating the strength of lattice-preferred orientation. *Tectonophysics*, **411**, 157–167.

STAUFFER, M. R. 1966. An empirical-statistical study of three-dimensional fabric diagrams as used in structural analysis. *Canadian Journal of Earth Sciences*, **3**, 473–498.

TOMMASI, A., MAINPRICE, D., CANOVA, G. & CHASTEL, Y. 2000. Viscoplastic self-consistent and equilibrium-based modeling of olivine lattice preferred orientations. 1. Implications for the upper mantle seismic anisotropy. *Journal of Geophsical Research*, **105**, 7893–7908.

ULRICH, S. & MAINPRICE, D. 2005. Does cation ordering in omphacite influence development of lattice-preferred orientation? *Journal of Structural Geology*, **27**, 419–431.

VOLLMER, F. W. 1990. An application of eigenvalue methods to structural domain analysis. *Geological Society of America Bulletin*, **102**, 786–791.

WATSON, G. S. 1983. *Statistics on Spheres*. J. Wiley and Sons, New York.

WATSON, G. S. 1966. The statistics of orientation data. *Journal of Geology*, **74**, 786–797.

WEISS, L. E. & WENK, H.-R. 1985. Symmetry of pole figures and textures. *In*: WENK, H.-R. (ed.) *Preferred Orientation in Deformed Metals and Rocks: An Introduction to Modern Texture Analysis*. Academic Press, London, 49–72.

WOODCOCK, N. H. 1977. Specification of fabric shapes using an eigenvalue method. *Geological Society of America Bulletin*, **88**, 1231, http://dx.doi.org/10.1130/0016-7606